On the stability of thermocapillary convection of a Bingham fluid in an infinite liquid layer

Kai-Xin Hu [a,*], Meng He [b], Qi-Sheng Chen [b,c], Rong Liu [d]

[a] *School of Mechanical Engineering and Mechanics, Ningbo University, Ningbo, Zhejiang 315211, China*
[b] *School of Engineering Science, University of Chinese Academy of Sciences, Beijing 100190, China*
[c] *Key Laboratory of Microgravity, Institute of Mechanics, Chinese Academy of Sciences, Beijing 100190, China*
[d] *School of Mechanical and Electrical Engineering, Gui Lin University of Electronic Technology, Gui Lin 541004, China*

ARTICLE INFO

ABSTRACT

The linear stability of thermocapillary liquid layer of a Bingham-plastic fluid is studied. Due to the yield stress of Bingham fluid, there is a plug region in the flow, which divides the yielded flow into two regions. When the flow is subjected to a small perturbation, the velocity perturbation below the upper surface of plug region is negligible, while the temperature perturbation can be found in all flow regions at moderate and small Prandtl numbers (Pr). The perturbation amplitude of the upper surface of plug region decreases rapidly with the increase of Pr. The preferred modes are the upstream oblique wave and the downstream streamwise wave at small and large Pr, respectively. The effects of the yield stress, gravity and the interfacial heat transfer on the flow stability are discussed. The perturbation amplitude only appears above the plug region, which differs from the cases in the plane Bingham–Poiseuille flow and the thermocapillary liquid layer of a Carreau fluid.

© 2018 Elsevier Ltd. All rights reserved.

1. Introduction

A liquid layer will be set in motion by a temperature-induced surface tension gradient when a horizontal temperature gradient is imposed on its surface. This flow is called the thermocapillary convection. Due to its important role in crystal growth [1], the thermocapillary convection has been studied extensively [2]. Recently, the thermocapillary flows of non-Newtonian fluids have also received much attention for its great practical importance in film coating [3], film drying [4], dewetting [5], lithography [6], inkjet printing [7] and polymer processing in microgravity [8]. The non-Newtonian effect makes the flow property vary considerably from that of a Newtonian fluid.

The viscoelastic thermocapillary liquid layers have been investigated by many authors [9–12]. It is found that although the elasticity does not change the velocity and temperature distributions in the basic flow, due to the normal stress, the flow stability is affected by the elasticity significantly. There are also a few papers devoted to the study of thermocapillary flows of shear-thinning fluids [13–15]. For linear flow, the shear-thinning effect does not change the basic flow, however, it is destabilizing at small and moderate Pr but increases the stability slightly at large Pr. For return flow, the shear-thinning effect leads to a viscosity

stratification in the basic flow, the streamwise wave is excited at large Pr, and a new mechanism is found at moderate Pr, where the hot spots appear at the bottom of the layer [15]. However, to the best of our knowledge, the thermocapillary liquid layer of viscoplastic fluids has not been investigated.

Viscoplastic fluids appear in many industrial applications and nature environment, such as drilling muds [16], polymers [17], mucus [18] and lava [19]. The main feature of a viscoplastic fluid is its yield stress: it exhibits liquid-like behaviour when it is sufficiently stressed, and solid-like behaviour when the stress is low. Due to the special property and wide applications, there are many works devoted to the study of viscoplastic fluids. The recent developments have been reviewed by Balmforth, Frigaard & Ovarlez [18].

One of the ideal models for viscoplastic fluids is the Bingham fluid, which exhibits a yield stress and a plastic viscosity [20]. The Bingham fluid has been widely used in theoretical studies for its simplicity [21]. In many Bingham fluid flows, there can be a region where the shear stress is less than the yield stress. It behaves as a rigid body and is called the plug region or unyielded region. The inclusion of a plug region makes the flow stability of a Bingham fluid quite different from those of other fluids.

The shear flow stabilities of Bingham fluids have been studied in many works, which indicate that the flow is stabilized by the effect of the yield stress. Frigaard, Howison & Sobey [16] have examined the stability of plane Poiseuille flow of a Bingham fluid, and found

---

Nomenclature

$\hat{a}$	thermal expansion coefficient
b	temperature gradient on the surface
$B = \tau_0 d/\mu_0 \hat{U}_0$	Bingham number
$Bi = \hat{h}d/\hat{k}$	Biot number
$Bo = \rho g \hat{a} d^2/\gamma$	dynamic Bond number
$c = -\sigma_i/k$	wave speed
d	depth of the layer
g	gravitational acceleration
h_0	length of the plug region
$h^{\pm}$	perturbations of the yield surface
$\hat{h}$	surface heat transfer coefficient
$k = \sqrt{\alpha^2 + \beta^2}$	wave number of wave propagation
$\hat{k}$	thermal conductivity
$Ma = b\gamma d^2/\mu_0\chi$	Marangoni number
$Pr = \mu_0/\rho\chi$	Prandtl number
$\tilde{Q}$	imposed heat flux to the environment
$R = \rho \hat{U}_0 d/\mu_0$	Reynolds number
$(\mathbf{u}, T, P, \boldsymbol{\tau})$	velocity, pressure, temperature and stress

$\hat{U}_0 = b\gamma d/\mu_0$	characteristic velocity
z_0	length of the yielded region
α, β	wave number in the x and y directions
γ	negative rate of change of surface tension with temperature
$\dot{\gamma} = \sqrt{\dot{\gamma}_{ij}\dot{\gamma}_{ij}/2}$	second invariant of $\dot{\gamma}$
$\dot{\boldsymbol{\gamma}}$	strain-rate tensor
$\delta/\delta t$	upper convected derivative
μ	dimensionless effective viscosity
μ_0	plastic viscosity
ρ	fluid density
$\tilde{\sigma}$	surface tension
σ_r, σ_i	growth rate and frequency of small perturbation
$\tau = \sqrt{\tau_{ij}\tau_{ij}/2}$	second invariant of $\boldsymbol{\tau}$
τ_0	yield stress
ϕ	propagation angle
χ	thermal diffusivity

that the critical Reynolds number increases almost linearly with increasing Bingham number. The nonlinear stability analysis has been performed by Nouar & Frigaard [22]. The results showed that the critical Reynolds number R increases like $R = O(B^{1/2})$ when the Bingham number $B \to \infty$. On the other hand, the three-dimensional linear stability analysis performed by Frigaard and Nouar [23] suggested that when $B \to \infty$, a critical Reynolds number $R = O(B^{3/4})$ is bounded for all wavelengths. The receptivity problem of plane Bingham–Poiseuille flow with respect to weak perturbations has been investigated using modal and non-modal approaches by Nouar et al. [24]. It has been reported that when $B \ll 1$, the optimal disturbance consists of almost streamwise vortices, whereas at moderate or large B, the optimal disturbance becomes oblique. Nouar & Bottaro [25] have revisited the problem for the case in which the idealized base flow is slightly perturbed. The results suggested that very weak defects are indeed capable to excite exponentially amplified streamwise travelling waves. The study of the stability of Bingham fluid flows has been extended to the spiral Couette flow [26] and Taylor-Couette flow [27].

The purpose of this paper is to examine the thermocapillary convection of a Bingham fluid in an infinite liquid layer and its stability, which have not been studied before. The works of Bingham fluid have demonstrated that the flow stability depends on the Bingham number obviously. So we have reasons to believe that there can be something new in the thermocapillary convection of a Bingham fluid, which are different from those in other fluids.

The paper is organized as follows. In Section 2, the physical model and numerical descriptions of the problem are presented. The basic flow solutions and perturbation equations are derived. Then in Section 3, critical parameters at different Bingham number, Bond number and Biot number are obtained; the perturbations of the velocity, temperature and yield surface are displayed and the energy mechanism is studied; the instability is discussed and comparisons are made with other fluids and flows. Finally, our conclusions are presented in Section 4.

2. Problem formulation

The model of thermocapillary liquid layer [28] is applied in the present work, where a fluid layer on an infinite rigid plane is subjected to a temperature gradient on the free surface. The instability behaviours predicted by this model have been observed in both experiment [29] and numerical simulation [30]. In Fig. 1, d is the

depth of the layer, U_0 is the velocity, x, y, z are the streamwise, spanwise and wall-normal directions, respectively. As the shear rate in the interior of the layer is smaller than that near the surface and wall, there will be a plug region in the middle of the layer. The flow consists of three regions: I and II are yielded regions where the shear stress is larger than the yield stress, while III is the unyielded or plug region. The ranges of I, II and III are $[0, z_0]$, $[z_0 + h_0, 1]$, and $(z_0, z_0 + h_0)$, respectively. Here, $0 < z_0 < z_0 + h_0 < 1$.
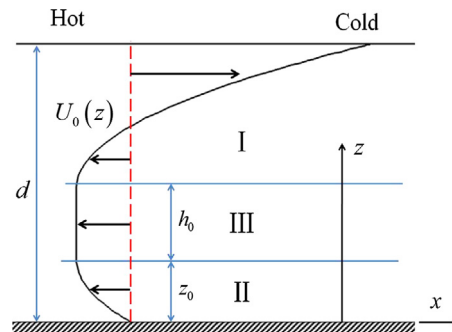
2.1. Governing equations

The scaled constitutive equation of a Bingham fluid can be written as follows [24],

$$\boldsymbol{\tau} = \mu\dot{\boldsymbol{\gamma}} \Longleftrightarrow \tau > \frac{B}{R}, \tag{2.1}$$

$$\dot{\gamma} = 0 \Longleftrightarrow \tau \leqslant \frac{B}{R}, \tag{2.2}$$

$$\mu = \frac{1}{R}\left(1 + \frac{B}{\dot{\gamma}}\right), \tag{2.3}$$

where $\boldsymbol{\tau}$ is the stress tensor, μ is the dimensionless effective viscosity, $\dot{\boldsymbol{\gamma}}$ is the strain-rate tensor with the form $\dot{\boldsymbol{\gamma}} = \nabla\mathbf{u} + (\nabla\mathbf{u})^{\mathrm{T}}$, $\mathbf{u} = (u, v, w)$ is the velocity, $\tau = \sqrt{\tau_{ij}\tau_{ij}/2}$ and $\dot{\gamma} = \sqrt{\dot{\gamma}_{ij}\dot{\gamma}_{ij}/2}$ are the

Fig. 1. The schematic of the thermocapillary liquid layer for a Bingham fluid. Here, I and II are yielded regions, III is the plug region, d is the depth of the layer, z_0 is the length of the yielded region II, h_0 is the length of the plug region, U_0 is the velocity field.

second invariant of τ and $\dot{\gamma}$, respectively. R and B are the Reynolds and Bingham numbers, respectively, which are defined as

$$R = \rho \hat{U}_0 d/\mu_0, B = \tau_0 d/(\mu_0 \hat{U}_0). \tag{2.4}$$

Here, d is the depth of the layer, ρ is the fluid density, μ_0 is the plastic viscosity, τ_0 is the yield stress, $\hat{U}_0$ is the characteristic velocity with the expression $\hat{U}_0 = b\gamma d/\mu_0$, where b is the temperature gradient on the surface and γ is the negative rate of change of surface tension with temperature. For many viscoplastic polymer melts, such as polyethylene, polystyrene and polyisobutylene [31], the surface tension is linearly dependent on the temperature [32]. So γ can be seen as a constant, which is similar to the case in Newtonian fluid [28].

In the presence of gravity, we use the Boussinesq approximation. The gravity effect can be quantified in terms of the dynamic Bond number $Bo = \rho g \hat{a} d^2/\gamma$, where $\hat{a}$ is the thermal expansion coefficient, and g is the gravitational acceleration[29].
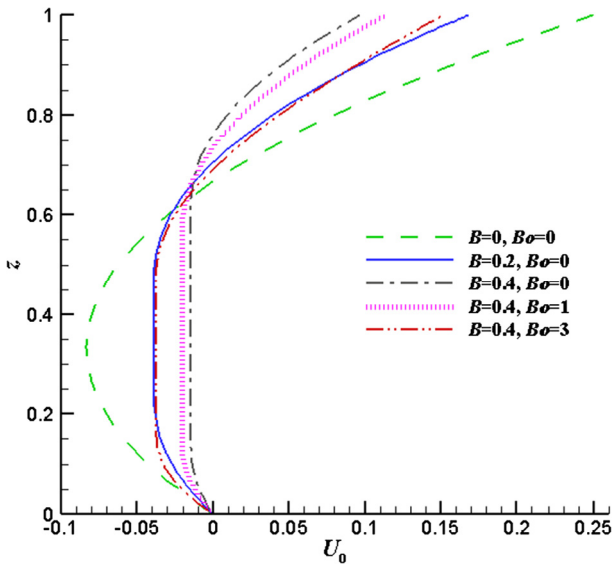

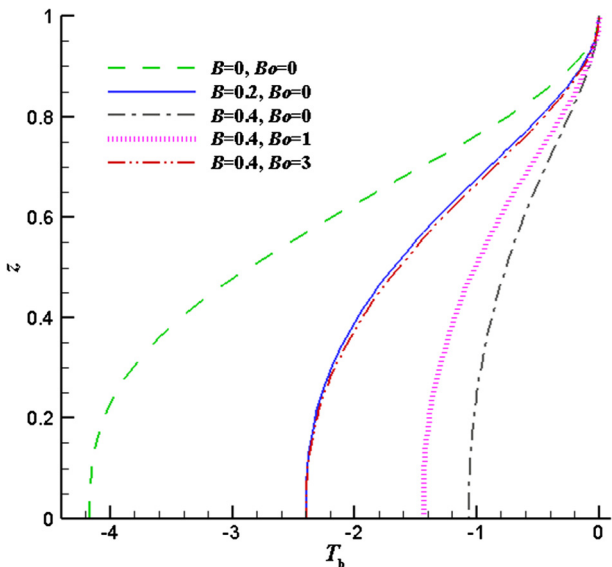**Fig. 2.** The velocity distributions in the return flow.

Fig. 3. The temperature distributions at $Ma = 200$ in the return flow.

For the thermocapillary liquid layer, the dimensionless forms of governing equations are

$$\nabla \cdot \mathbf{u} = 0, \tag{2.5}$$

$$\frac{\partial \mathbf{u}}{\partial t} + \mathbf{u} \cdot \nabla \mathbf{u} = -\nabla p + \nabla \cdot \tau + \frac{Bo}{R} \cdot T\mathbf{e}_3, \tag{2.6}$$

$$\frac{\partial T}{\partial t} + \mathbf{u} \cdot \nabla T = \frac{1}{Ma} \nabla^2 T, \tag{2.7}$$

which are the continuity equation, momentum equation [33] and energy equation [28], respectively. The momentum Eq. (2.6) is used for Bingham fluid, where the relation between τ and $\dot{\gamma}$ in ((2.1)–(2.3)) is far more complex than that for Newtonian fluid ($\tau \propto \dot{\gamma}$) in Refs. [28,33]. Here, $Ma = b\gamma d^2/(\mu_0 \chi)$ is the Marangoni number, χ is the thermal diffusivity. The relation between Ma and R is $Ma = R \cdot Pr$, where $Pr = \mu_0/(\rho \chi)$ is the Prandtl number. p and T stand for the pressure and temperature, respectively. The boundary conditions are

$$u = v = w = 0, \frac{\partial T}{\partial z} = 0, z = 0, \tag{2.8}$$

$$\tau_{13} + \frac{1}{R}\frac{\partial T}{\partial x} = 0, \tau_{23} + \frac{1}{R}\frac{\partial T}{\partial y} = 0, w = 0,$$

$$-\frac{\partial T}{\partial z} = Bi \cdot (T - T_\infty) + \tilde{Q}, z = 1. \tag{2.9}$$

Here, $Bi = \hat{h}d/\hat{k}$ is the Biot number, where $\hat{h}$ and $\hat{k}$ are the surface heat transfer coefficient and the thermal conductivity, respectively. T_∞ is the temperature of the bounding gas far from the surface. $\tilde{Q}$ is

Table 1
The critical parameters in the thermocapillary liquid layer of a Newtonian fluid at $Pr = 13.9, Bo = 0.142$. Here, the definition of Marangoni number is the same as that in Ref. [33], and $\psi = 180^0 - \phi$.

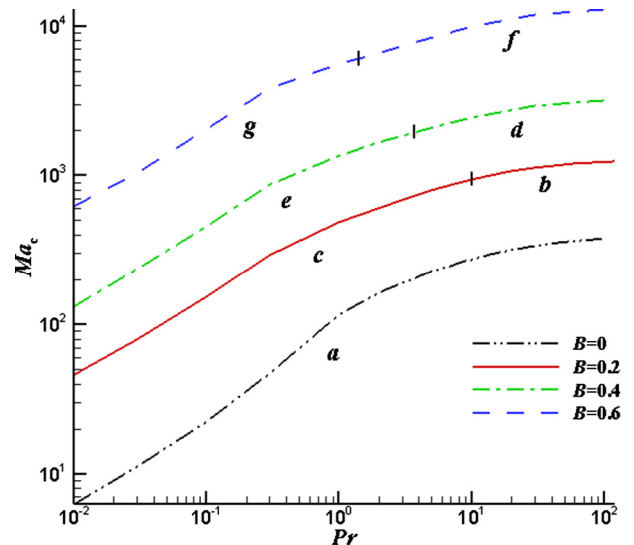| | Experiment | Linear stability analysis | |
	Riley and Neitzel [29]	Chan and Chen [33]	Present work
Ma	26.91	24.70	24.72
ψ	23.2°	21.7°	21.9°
k	2.58	2.48	2.47
$|\sigma_i|$	0.0217	0.0237	0.0234
c	0.0561	0.0583	0.0579

Fig. 4. The variation of Ma_c with Pr at $Bo = 0$, $Bi = 0$. The curves correspond to oblique waves: (a), (c), (e), (g), and streamwise waves: (b), (d), (f).
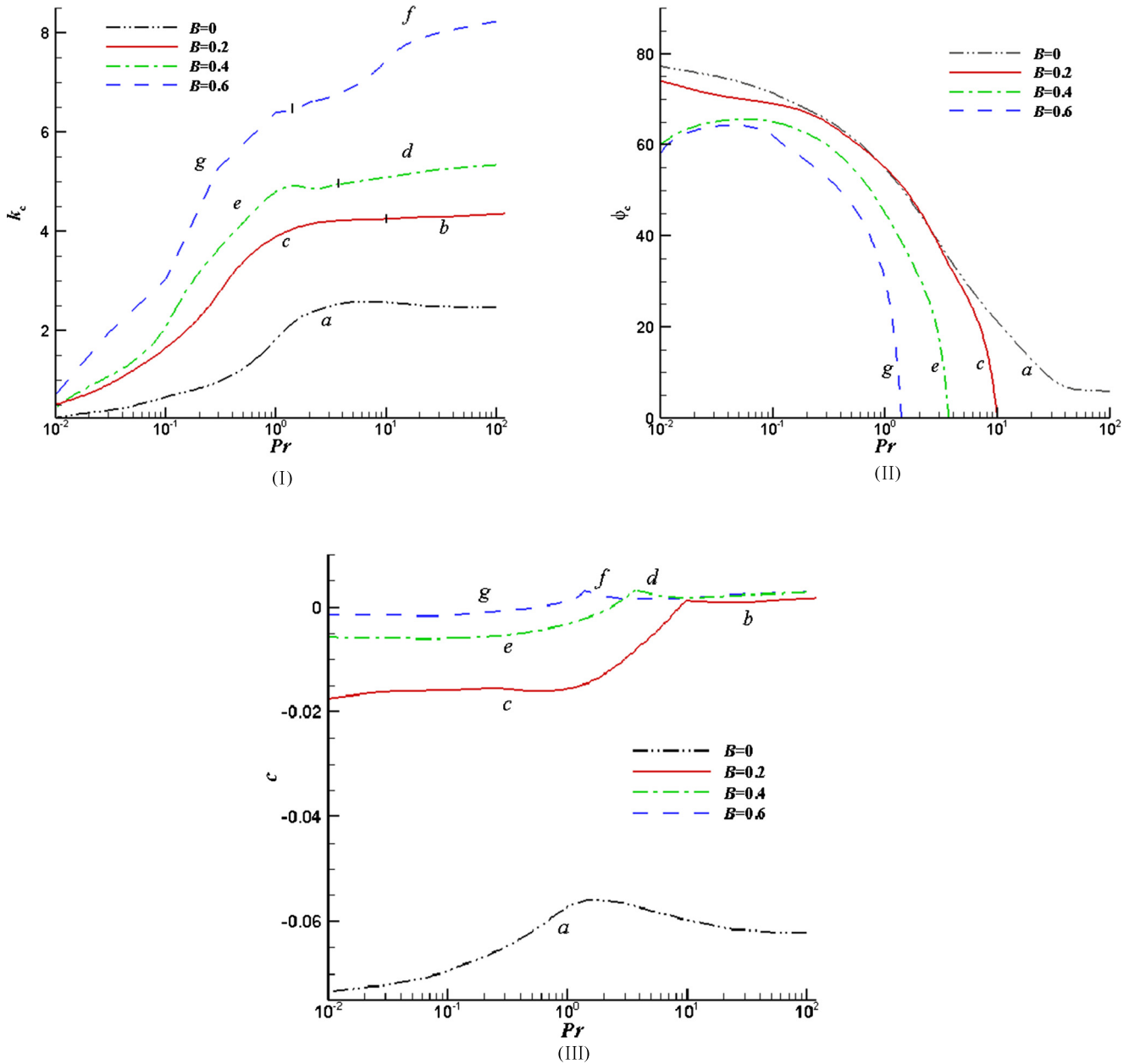
Fig. 5. The (I) wave number, (II) wave propagation angle and (III) wave speed corresponding to the waves in Fig. 4.

the heat flux to the environment, which is introduced for the energy balance on the surface.

We consider the case when the basic flow is parallel and its temperature is linear in x as imposed plus a distribution in z:

$$\mathbf{u} = (U_0(z), 0, 0), T_0(x, z) = -x + T_b(z), \tag{2.10}$$

where $T_b(1) = 0$. T_∞ has the form $T_\infty = -x$ [28].

The linear flow ($U_0(z) = z$) of a Bingham fluid is similar to that of a Carreau fluid [15], so we do not discuss it separately and restrict our attention to the case of return flow, which has zero mass flux in the vertical section,

$$\int_0^1 U_0(z) dz = 0. \tag{2.11}$$

Then, the heat flux $\tilde{Q}$ can be determined by the basic flow solution: $\tilde{Q} = -\frac{\partial T_0}{\partial z}\big|_{z=1} - Bi \cdot (T_0|_{z=1} - T_\infty)$, where $\frac{\partial T_0}{\partial z}\big|_{z=1} = \frac{\partial T_0}{\partial z}\big|_{z=0} + \int_0^1 \frac{\partial^2 T_0}{\partial z^2} dz = -Ma \int_0^1 u(z) dz$. As $T_0|_{z=1} = T_\infty = -x$, $\tilde{Q} = 0$ for return flow.

The solution of the return flow can be derived numerically, where the details are described in Appendix A. The distributions of velocity and temperature are displayed in Figs. 2 and 3, respectively. The length of the plug region increases with B, whereas both the surface velocity and the vertical temperature gradient decrease with B. However, Bo and B have the opposite effects on the velocity and temperature.

2.2. Linear stability analysis

Considering an infinitesimal perturbation added to the basic flow,

$$(\mathbf{u}, T, P, \boldsymbol{\tau}) = (\mathbf{u}_0, T_0, P_0, \boldsymbol{\tau}_0) + \varepsilon(\mathbf{u}', T', P', \boldsymbol{\tau}'), \tag{2.12}$$

with $\varepsilon \ll 1$. The yield surface positions $z_Y^\pm$ will also be perturbed from their initial positions,

$$z_Y^- = z_0 - \varepsilon h^-, z_Y^+ = z_0 + h_0 + \varepsilon h^+. \tag{2.13}$$

The relation between u and $h^{\pm}$ is [23]:

$$Du = \begin{cases} -h^- D^2 U_0(z), z = z_0, \\ -h^+ D^2 U_0(z), z = z_0 + h_0. \end{cases} \quad (2.14)$$

The perturbation is assumed to vary periodically along the streamwise and spanwise directions,

$$(\mathbf{u}', T', P', \boldsymbol{\tau}', h^{\pm}) = (\widehat{u}, \widehat{v}, \widehat{w}, \widehat{T}, \widehat{P}, \widehat{\boldsymbol{\tau}}, \widehat{h^{\pm}}) \exp[\sigma t + i(\alpha x + \beta y)], \quad (2.15)$$

where $\sigma = \sigma_r + i\sigma_i$, σ_r and σ_i are the growth rate and frequency, respectively. α and β are the wave number in the x and y directions, respectively. The wave number, the propagation angle and wave speed are defined as $k = \sqrt{\alpha^2 + \beta^2}$, $\phi = \tan^{-1}(\beta/\alpha)$, $c = -\sigma_i/k$, respectively. In the above equations, the subscript 0 stands for the basic flow. Hereafter, the variables without the subscript 0 are perturbations.

Then the perturbation equations are derived, whose details are described in Appendix B. They can be solved by the Chebyshev-collocation method [34], and the eigenvalues σ are obtained by using the QZ algorithm available in the Matlab-software package. In our work, the results are sufficiently accurate when the number of Chebyshev nodes is about $90 - 120$.

2.3. Code validation

The code for the perturbation Eqs. (B.1-B.10) is rewritten on the basis of the Matlab code for hydrodynamic stability calculations in the Appendix of Ref. [34]. If we set $B = 0$ and delete the constraint in the plug region (B.4) in the code, then the case of Newtonian fluid is recovered. Thus, the code can be validated by solving the same problems of Newtonian fluid in Ref. [33]. In Table 1, comparisons are made with the experiment and the computation, which shows that our results agree with the values in previous works.

3. Numerical results

We compute the Marangoni number Ma_N of neutral modes ($\sigma_r = 0$) and determine the critical Marangoni number Ma_c, which is defined as follows,

$$Ma_c = \min_{\alpha, \beta} Ma_N(Pr, B, Bo, Bi). \quad (3.1)$$

3.1. Critical parameters

The variation of Ma_c with Pr at $Bo = 0$, $Bi = 0$ is displayed in Fig. 4. It can be seen that Ma_c increases with B and Pr significantly. Physically, B increases with the yield stress, which can stabilize the flow. When Pr is large enough, the preferred mode changes from the oblique wave ($\phi \in (0°, 90°)$) to the two-dimensional streamwise wave ($\phi = 0°$).

The wave number, propagation angle and wave speed corresponding to the modes in Fig. 4 are displayed in Fig. 5. The wave number increases with B, especially when Pr is large. In contrast, the wave propagation angle decreases with B. The wave speed increases with B, and changes from negative (upstream wave) to positive (downstream wave) when Pr is large enough. $|c|$ in the Bingham fluid ($B > 0$) is far less than that in the Newtonian fluid ($B = 0$).

Then we study the effects of Bo and Bi. The variations of Ma_c with Pr for several values of Bo and Bi are displayed in Fig. 6. The flow is destabilized by Bo at small Pr, but stabilized at large Pr. When $Bo = 3$, another kind of streamwise wave is excited at large Pr. Ma_c always increases with Bi, and the relative change is more obvious at small Pr. The computation shows that the variation of
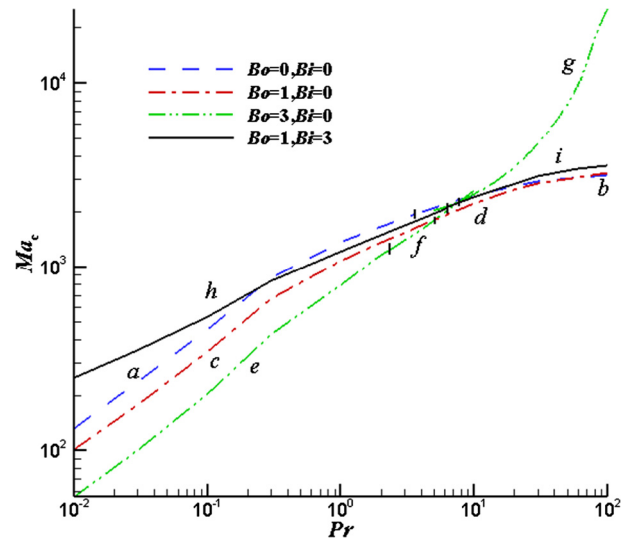

Fig. 6. The variation of Ma_c with Pr at $B = 0.4$. The curves correspond to oblique waves: (a), (c), (e), (h), and streamwise waves: (b),(d), (f),(g),(i).

Ma_c with Bi is obvious when $Bi \geqslant 3$. For simplicity, we restrict our attention to the case at $Bi = 3$.

The wave number, propagation angle and wave speed corresponding to the modes in Fig. 6 are displayed in Fig. 7. The effect of Bo for k_c is similar to that for Ma_c. When $Bo = 1$, the variation of ϕ_c with Bo is rather small. When $Bo = 3$, ϕ_c increases a little at $Pr \leqslant 2$, but decreases at $Pr > 2$. When Pr is small, both the wave number and the propagation angle increases with Bi significantly. The effects of Bo and Bi for the wave speed are similar to those for Ma_c.

3.2. Energy analysis

The energy mechanism of the instability can be seen from the perturbation energy growth, which is derived as follows,

$$\frac{\partial E_{kin}}{\partial t} = -\frac{1}{2} \int (\boldsymbol{\tau} : \dot{\boldsymbol{\gamma}}) d^3 r + \int \mathbf{u} \cdot \boldsymbol{\tau} \cdot \mathbf{n} d^2 r - \int \mathbf{u} \cdot ((\mathbf{u} \cdot \nabla) \mathbf{u}_0) d^3 r$$
$$+ \int \left(\frac{Bo}{R} \cdot T \mathbf{e}_3 \cdot \mathbf{u} \right) d^3 r = -N + M + I + G,$$

(3.2)

where N is the work done by the perturbation stress, M is the work done by Marangoni forces on the surface, I is the energy from the basic flow, and G is the work done by gravity, respectively.

When $Bo = 0$, M and I are the energy source for the perturbation while N is the viscous dissipation. I/N decreases with B. The reason is that the perturbation can only absorb energy from the basic flow in the yielded region I. When B increases, both the length of region I and the vertical velocity gradient dere
ase, which will reduce the energy from the basic flow.

The ratios I/N and G/N for the neutral mode at $B = 0.4$ are displayed in Fig. 8. It can be seen that I/N increases with Bi significantly when Pr is small. I becomes the largest energy source at $Bi = 3, Pr = 0.01$. G/N decreases slightly with Bi. The variation of I/N with Bo is not obvious. G/N decreases with Pr at $Bo = 1$. However, when $Bo = 3$, G/N reaches a minimum at $Pr \approx 3$.

3.3. The perturbation of the flow field

The perturbations of the flow field are displayed in Figs. 9–13. Here, the amplitude of temperature perturbation is normalized. It can be seen that most of the velocity perturbation is in the yielded
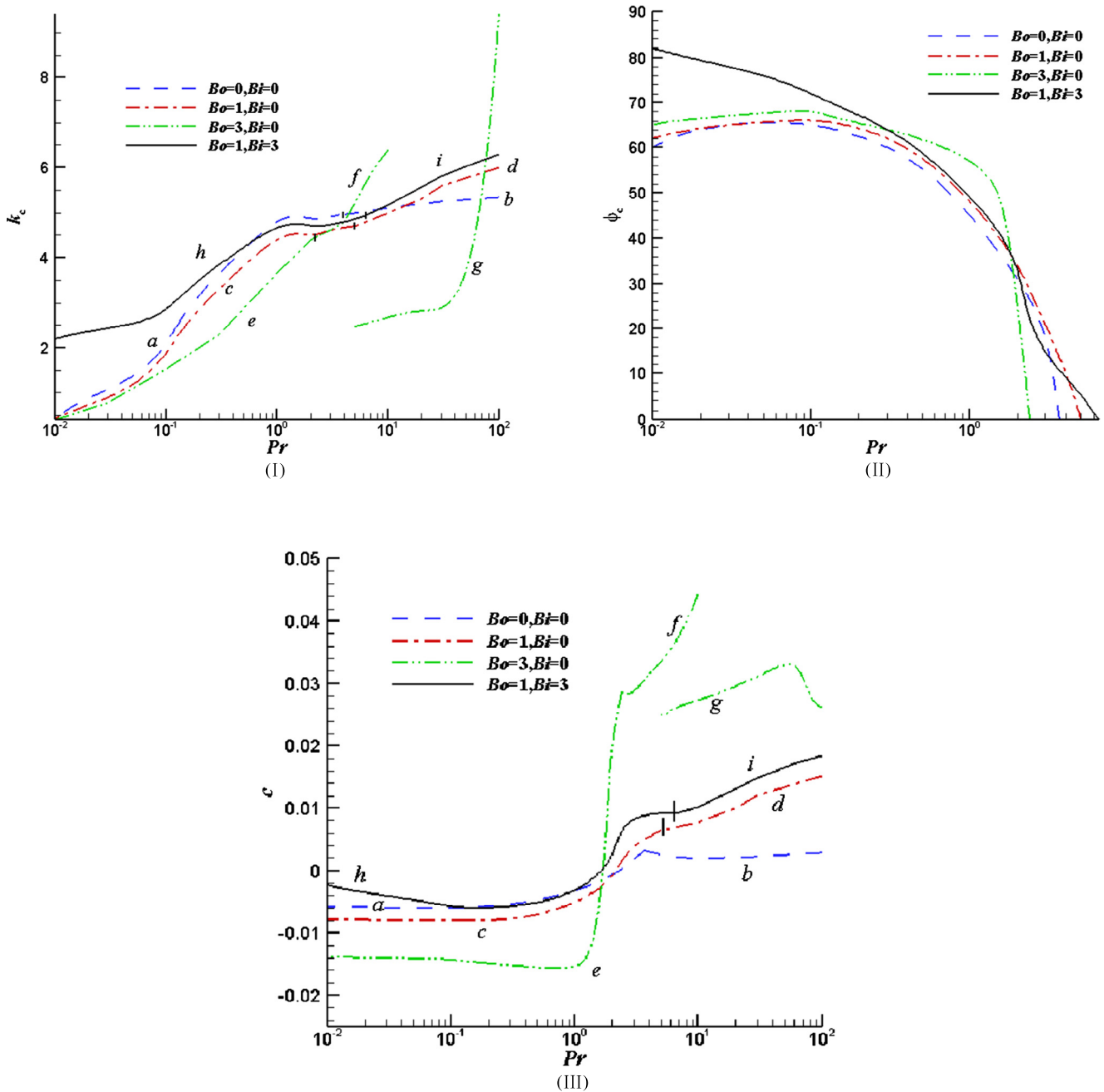
Fig. 7. The (I) wave number, (II) wave propagation angle and (III) wave speed corresponding to the waves in Fig. 6. As the wave speed of (g) is far larger than others, we show $c/10$ for (g) in (III).

region I. However, the distribution of the temperature perturbation depends on Pr. For large Pr, the temperature perturbation is concentrated in the yielded region I, whereas for moderate and small Pr, we can see the temperature perturbation is below the upper surface of plug region. The perturbation amplitude of the upper surface of plug region decreases rapidly with Pr.

In Fig. 12, the streamlines near the hot spot are clockwise, and almost coincide with the isothermals. In contrast, in Figs. 9–11 and 13, the corresponding streamlines are counterclockwise. This phenomenon is similar to the case at $Bo = 3$ in a Carreau fluid. It can be seen by comparing Figs. 9 and 12 that the perturbation amplitude of the upper surface of plug region in Fig. 12 is an order of magnitude larger that in Fig. 9, which indicates that the gravity can obvi-

ously increase the perturbation of the upper surface of plug region at large Pr. However, the effect of gravity for h^+ at moderate and small Pr is not obvious.

It can be seen by comparing Figs. 11 and 13 that the Biot number can decrease the temperature perturbation near the surface significantly. Meanwhile, the perturbation amplitude of the upper surface of plug region in Fig. 13 is larger than that in Fig. 11, although they have the same order. Suppose a perturbation in Fig. 11 is added to the flow at $Bi = 3$, then due to the heat transfer to the gas, the temperature perturbation decreases. A larger velocity perturbation is needed to maintain the amplitude of temperature perturbation. Then the velocity gradient on the upper surface of plug region increases.
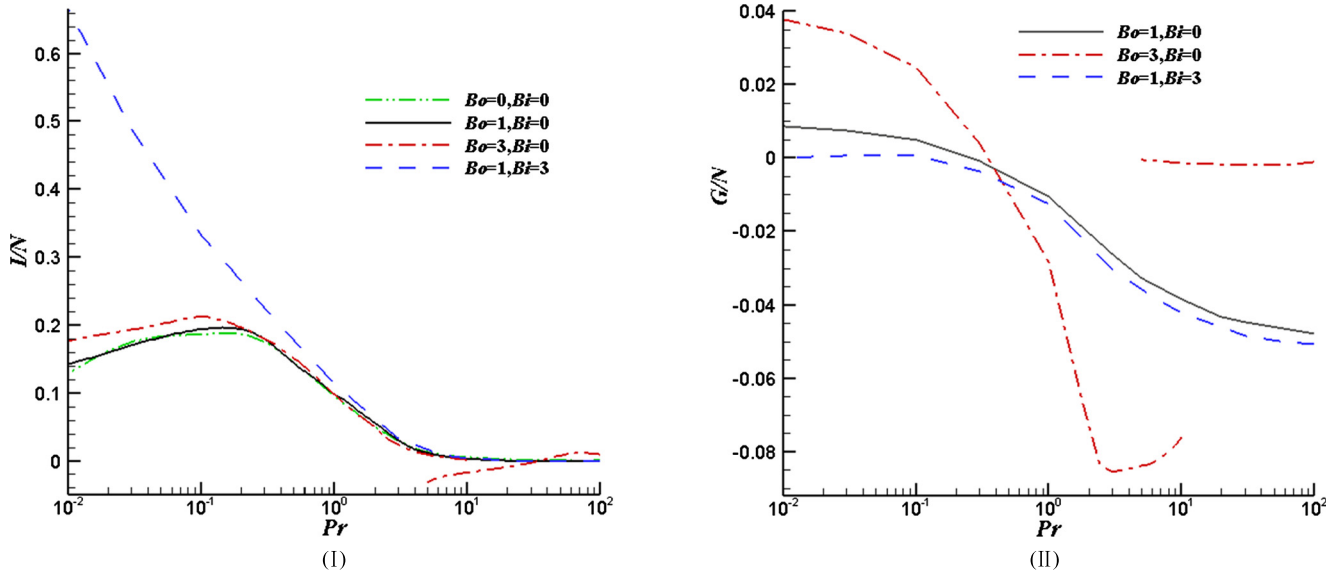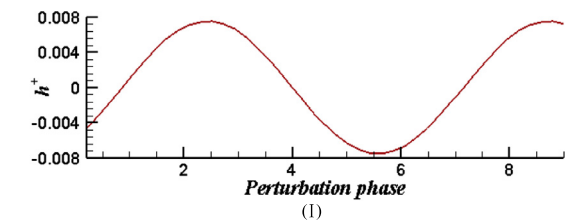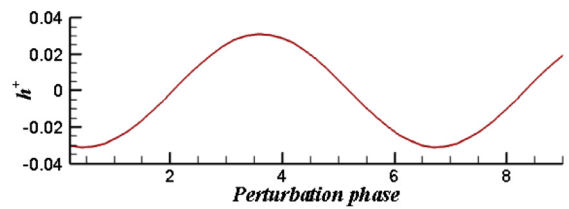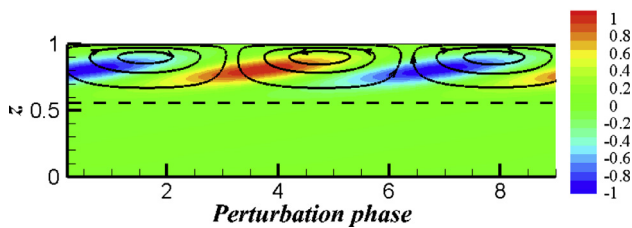
Fig. 8. The ratios I/N and G/N for the neutral mode at $B = 0.4$.

Fig. 9. The perturbation flow field of the neutral mode at $Pr = 30$, $B = 0.4$, $Bo = 1$, $Bi = 0$: (I) the perturbation of the upper surface of plug region; (II) the streamlines and isothermals. The dashed line is the upper surface of plug region. t-T.

Fig. 10. The perturbation flow field of the neutral mode at $Pr = 1$, $B = 0.4$, $Bo = 1$, $Bi = 0$: (I) the perturbation of the upper surface of plug region; (II) the streamlines and isothermals.

3.4. Discussion

For large Pr, all the perturbations are restricted in the yielded region I. The upper surface of plug region is the same as a solid wall. Thus, the instability that appears in the yielded region I is similar to that in the return flow of a shear-thinning fluid [15]. The difference between them is that the mass flux in the yielded region I is larger than that of the return flow. Therefore, in the return flow without gravity, there can be downstream waves in a Bingham fluid while the perturbations waves are always upstream in a shear-thinning fluid [15]. For small Pr, the wave speed increases obviously with B (see Fig. 5). However, the waves are still upstream. The perturbations at small Pr are nearly spanwise, so the increase of the mass flux in streamwise direction does not change ϕ_c obviously.

The reason why the distribution of the temperature perturbation depends on Pr can be seen as follows. For large Pr, the temperature distribution mainly depends on the heat convection. In the region where there is no velocity perturbation, the temperature perturbation is also negligible (see Figs. 9 and 12). However, for small Pr, the heat conduction is more important, so the temperature below the upper surface of plug region is affected by the temperature perturbation in the yielded region I significantly (see Figs. 11 and 13).

The perturbation amplitude of the upper surface of plug region decreases with Pr (see Figs. 9–13). This can be seen from (2.14) that h^+ is linear with Du. For large Pr, most of the perturbation energy comes from the Marangoni forces. The velocity perturbations are concentrated near the surface. So the velocity gradient across the upper surface of plug region is very small. However, for small Pr, the perturbation also absorbs energy from the basic flow, the perturbation velocity in the interior is not negligible. The velocity gradient on the upper surface of plug region is far larger than that at large Pr.

Both the thermocapillary liquid layer and the plane Poiseuille flow are parallel shear flows. For a Bingham fluid, there is a plug
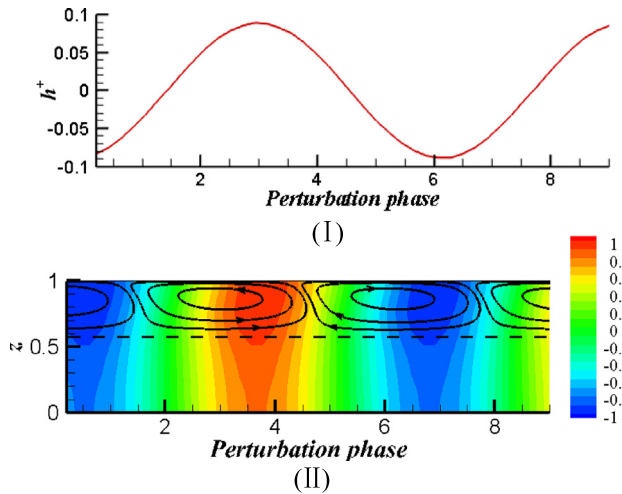
Fig. 11. The perturbation flow field of the neutral mode at $Pr = 0.03$, $B = 0.4$, $Bo = 1$, $Bi = 0$: (I) the perturbation of the upper surface of plug region; (II) the streamlines and isothermals.
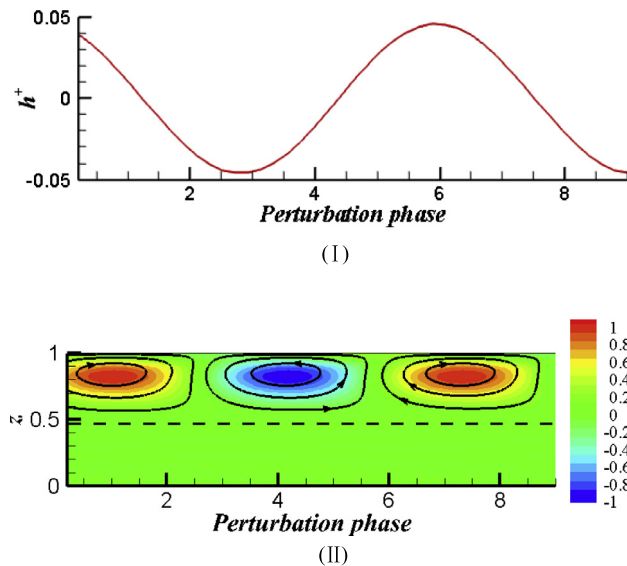

Fig. 12. The perturbation flow field of the neutral mode at $Pr = 30$, $B = 0.4$, $Bo = 3$, $Bi = 0$:(I) the perturbation of the upper surface of plug region; (II) the streamlines and isothermals.

region in the flow for both of them. However, a big difference is that the plane Poiseuille flow is symmetric with respective to its center line [16], while the thermocapillary liquid layer is not symmetric (see Fig. 1). Meanwhile, the temperature field is important for the latter (see Figs. 1 and 3), and there can be temperature perturbations in all three regions (see the isothermals in Figs. 9–13), which are not considered in the former. Furthermore, the energy mechanisms of these two flows are entirely different. In plane Poiseuille flow, the perturbation energy comes from the basic flow, and the velocity perturbation appears in two yielded regions. However, in the thermocapillary liquid layer, the work done by Marangoni forces on the surface is the main energy source for the instability. Therefore, the kinetic energy of the perturbation is concentrated near the surface, and there is little velocity perturbation below the upper surface of plug region (see the streamlines in Figs. 9–13).

The Bingham fluid is similar to the Carreau fluid to some extent. The viscosity depends on the shear rate and decreases significantly
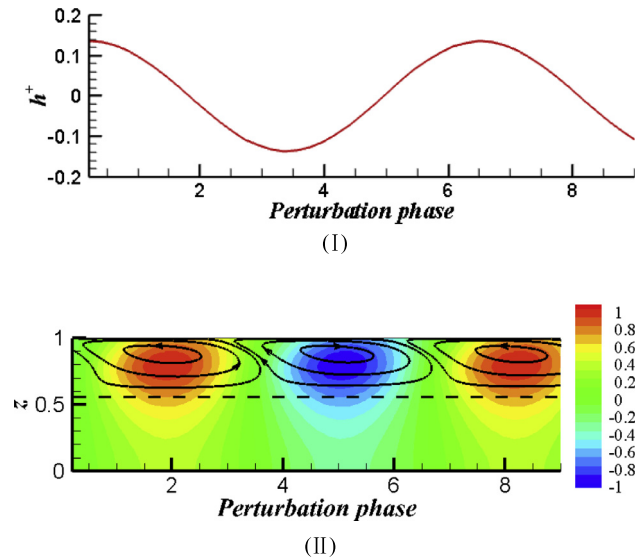

Fig. 13. The perturbation flow field of the neutral mode at $Pr = 0.03$, $B = 0.4$, $Bo = 1$, $Bi = 3$: (I) the perturbation of the upper surface of plug region; (II) the streamlines and isothermals.

when the shear rate is large enough for both of them. Therefore, we can make a comparison between the thermocapillary liquid layer of a Bingham fluid and that of a Carreau fluid. In the return flow, the variation of Ma_c with B and Pr in a Bingham fluid (see Fig. 4) is similar to that in a Carreau fluid [15], and the streamwise wave is excited at large Pr for both fluids. However, the instability of a Carreau fluid has hot spots at the bottom of the layer at moderate Pr [15]. In contrast, the hot spots are above the upper surface of plug region in a Bingham fluid (see Figs. 9–13), and the temperature perturbation below the upper surface of plug region is only caused by heat conduction. Additionally, in the case without gravity, the streamwise wave in a Bingham fluid is downstream (see (b), (d), (f) in Fig. 5) while that in a Carreau fluid is upstream [15].

4. Conclusion

In this work, the instability for a Bingham-fluid thermocapillary convection in an infinite liquid layer has been studied. The solution of the basic flow has been derived numerically. The effects of the yield stress (B), gravity (Bo) and the interfacial heat transfer (Bi) on the flow stability have been analysed comprehensively.

The return flow of a Bingham fluid consists of three regions, where the plug region is in the middle and others are yielded regions. When the Bingham number increases, the length of the plug region increases, but the vertical temperature gradient decreases. The velocity perturbation below the upper surface of plug region is negligible. However, the temperature perturbation appears in the whole flow region when the Prandtl number is not large. Meanwhile, the perturbation amplitude of the upper surface of plug region decreases rapidly with the increase of Pr.

Both the critical Marangoni number and wave number increase with B. The preferred mode becomes the downstream wave when the Prandtl number is large enough. The gravity can reduce the length of the plug region and increase the vertical velocity gradient. For large Pr, both the perturbation of the upper surface of plug region and the critical Marangoni number increase significantly with the gravity, whereas the work done by gravity for the perturbation is nearly zero. When the Biot number increases, the flow is stabilized and the basic flow becomes the largest energy source for the perturbation at small Pr.

For Bingham fluid flows, there is a plug region in both the thermocapillary liquid layer and the plane Poiseuille flow. However, the former has little velocity perturbation below the upper surface of plug region, while the velocity perturbation appears in two yielded regions for the latter. There is a big difference between the thermocapillary liquid layer of a Carreau fluid and that of a Bingham fluid. The instability for the former has hot spots at the bottom of the layer at moderate Pr, while the hot spots are above the plug region for the latter.

Conflict of interest statement

Acknowledgments

Appendix A. The derivation of the basic flow

We can substitute the form of basic flow (2.10) into the momentum Eq. (2.6). For the yielded regions (I and II), the momentum equation in x and z directions are derived as follows.

$$-\frac{\partial p}{\partial x} + \frac{\partial \tau_{13}}{\partial z} = 0, \tag{A.1}$$

$$-\frac{\partial p}{\partial z} + \frac{\partial \tau_{13}}{\partial x} + \frac{Bo}{R} \cdot T = 0. \tag{A.2}$$

As the velocity only depends on z: $U_0 = U_0(z)$, then

$$\boldsymbol{\tau} = \boldsymbol{\tau}(z), \frac{\partial \tau_{13}}{\partial x} = 0, \frac{\partial^2 p}{\partial x \partial z} = -\frac{Bo}{R} = \frac{\partial^2 \tau_{13}}{\partial z^2}. \tag{A.3}$$

Therefore,

$$R\tau_{13} = -\frac{Bo}{2}z^2 + C_1 z + C_2. \tag{A.4}$$

Denoting $D = d/dz$, the relation between of shear stress and velocity is

$$\begin{aligned} R\tau_{13} &= -B + DU_0(z), z \in [0, z_0] \\ DU_0(z) &= 0, (z_0, z_0 + h_0) \\ R\tau_{13} &= B + DU_0(z), z \in [z_0 + h_0, 1] \end{aligned} \tag{A.5}$$

where the constants C_1, C_2, z_0, h_0 and the velocity of basic flow can be obtained numerically with the following conditions: (A.6), (A.7).
The shear stress has

$$R\tau_{13} = \begin{cases} 1, z = 1 \\ B, z = z_0 + h_0 \\ -B, z = z_0 \end{cases} \tag{A.6}$$

and the velocity has

$$\int_0^1 U_0(z)dz = 0, U_0(z)|_{z=0} = 0. \tag{A.7}$$

Substituting (2.9) into (2.6), the temperature of basic flow must satisfy

$$-U_0(z) = \frac{1}{Ma}D^2 T_b(z). \tag{A.8}$$

This equation can be solved with the boundary conditions of the temperature.

Appendix B. The governing equations of perturbations

Substituting (2.15) into governing Eqs. (2.5-2.7), the linearized perturbation equations can be derived as follows. The equations for the perturbation velocity in the yielded regions are [15]

$$i\alpha\widehat{u} + i\beta\widehat{v} + D\widehat{w} = 0, \tag{B.1}$$

$$\begin{aligned} &\beta(\widehat{w}DU_0 + U_0 i\alpha\widehat{u}) - \alpha(U_0 i\alpha\widehat{v}) \\ &- \beta(i\alpha\widehat{\tau}_{11} + i\beta\widehat{\tau}_{12} + D\widehat{\tau}_{13}) + \alpha(i\alpha\widehat{\tau}_{12} + i\beta\widehat{\tau}_{22} + D\widehat{\tau}_{23}) = -\sigma(\beta\widehat{u} - \alpha\widehat{v}), \end{aligned} \tag{B.2}$$

$$\begin{aligned} &\alpha(D\widehat{w} \cdot DU_0 + \widehat{w}D^2 U_0 + DU_0 \cdot i\,\alpha\widehat{u} + U_0 i\,\alpha D\widehat{u}) \\ &+ \beta(DU_0 \cdot i\,\alpha\widehat{v} + U_0 i\,\alpha D\widehat{v}) - ik^2(U_0 i\alpha\widehat{w}) \\ &- (i\alpha^2 D\widehat{\tau}_{11} + 2i\alpha\beta D\widehat{\tau}_{12} + \alpha D^2\widehat{\tau}_{13} + i\beta^2 D\widehat{\tau}_{22} + \beta D^2\widehat{\tau}_{23}) \\ &+ ik^2(i\,\alpha\widehat{\tau}_{13} + i\beta\widehat{\tau}_{23} + D\widehat{\tau}_{33} + Bo \cdot \widehat{T}/R) = -\sigma(\alpha D\widehat{u} + \beta D\widehat{v} - ik^2\widehat{w}), \end{aligned} \tag{B.3}$$

while in the plug region, the perturbation velocity is zero,

$$\widehat{u} = \widehat{v} = \widehat{w} = 0, z \in (z_0, z_0 + h_0). \tag{B.4}$$

The equations for the perturbation temperature and stress are

$$\begin{aligned} &Ma\left(\widehat{u}\frac{\partial T_0}{\partial x} + \widehat{w}\frac{\partial T_0}{\partial z} + U_0 i\alpha\widehat{T}\right) + (\alpha^2 + \beta^2)\widehat{T} - D^2\widehat{T} \\ &= -\sigma Ma\widehat{T}, \end{aligned} \tag{B.5}$$

$$\widehat{\tau}_{11} - \mu_1 2i\alpha\widehat{u} = 0, \widehat{\tau}_{12} - \mu_1(i\alpha\widehat{v} + i\beta\widehat{u}) = 0,$$
$$\widehat{\tau}_{13} - \mu_2(D\widehat{u} + i\alpha\widehat{w}) = 0, \tag{B.6}$$

$$\widehat{\tau}_{22} - \mu_1(2i\beta\widehat{v}) = 0, \widehat{\tau}_{23} - \mu_1(i\beta\widehat{w} + D\widehat{v}) = 0, \widehat{\tau}_{33} - \mu_1(2D\widehat{w}) = 0. \tag{B.7}$$

Here,

$$\mu_1 = \frac{1}{R}\left(1 + \frac{B}{|DU_0|}\right), \mu_2 = \frac{1}{R}. \tag{B.8}$$

The linearized boundary conditions are

$$\widehat{u} = \widehat{v} = \widehat{w} = \frac{\partial\widehat{T}}{\partial z} = 0, z = 0, \tag{B.9}$$

$$\widehat{\tau}_{13} + \frac{1}{R}i\alpha\widehat{T} = 0, \widehat{\tau}_{23} + \frac{1}{R}i\beta\widehat{T} = 0, \widehat{w} = 0, \frac{\partial\widehat{T}}{\partial z} + Bi \cdot \widehat{T} = 0, z = 1. \tag{B.10}$$

References

[1] T. Dufar (Ed.), Crystal Growth Processes Based on Capillarity: Czochralski, Floating Zone, Shaping and Crucible Techniques, John Wiley & Sons, 2010.
[2] M.F. Schatz, G.P. Neitzel, Experiments on thermocapillary instabilities, Annu. Rev. Fluid Mech. 33 (1) (2001) 93–127.
[3] W.R. Hu, N. Imaishi, Thermocapillary flow in an annular liquid layer painted on a moving fiber, Int. J. Heat Mass Transfer 43 (24) (2000) 4457–4466.
[4] G. Toussaint, H. Bodiguel, F. Doumenc, B. Guerrier, C. Allain, Experimental characterization of buoyancy-and surface tension-driven convection during the drying of a polymer solution, Int. J. Heat Mass Transfer 51 (17) (2008) 4228–4237.
[5] J.P. Singer, S.E. Kooi, E.L. Thomas, Focused laser-induced marangoni dewetting for patterning polymer thin films, J. Polym. Sci. Pol. Phys. 54 (2016) 225–236.

[6] A.A. Darhuber, J.M. Davis, S.M. Troian, W.W. Reisner, Thermocapillary actuation of liquid flow on chemically patterned surfaces, Phys. Fluids 15 (5) (2003) 1295–1304.

[7] O.A. Basaran, H. Gao, P.P. Bhat, Nonstandard inkjets, Annu. Rev. Fluid Mech. 45 (2013) 85–113.

[8] J.P. Downey, J.A. Pojman, Polymer Research in Microgravity: Polymerization and Processing, American Chemical Society, Washington, DC, 2001.

[9] L.A. Davalos-Orozco, A.E. Chavez, Thermocapillary convection in a viscoelastic fluid layer under a horizontal temperature gradient, J. Appl. Polym. Sci. 49 (1991) 141–153.

[10] M.X. Tong, L.J. Yang, Q.F. Fu, Thermocapillar instability of a two-dimensional viscoelastic planar liquid sheet in surrounding gas, Phys. Fluids 26 (2014) 033105.

[11] I.J. Hernández-Hernández, L.A. Dávalos-Orozco, Competition between stationary and oscillatory viscoelastic thermocapillary convection of a film coating a thick wall, Int. J. of Therm. Sci. 89 (2015) 164–173.

[12] K.X. Hu, M. He, Q.S. Chen, Instability of thermocapillary liquid layers for Oldroyd-B fluid, Phys. Fluids 28 (3) (2016) 033105.

[13] Z. Alloui, P. Vasseur, Onset of Marangoni convection and multiple solutions in a power-law fluid layer under a zero gravity environment, Int. J. Heat Mass Transfer 58 (1) (2013) 43–52.

[14] C.H. Chen, Marangoni effects on forced convection of power-law liquids in a thin film over a stretching surface, Phys. Lett. A 370 (1) (2007) 51–57.

[15] K.X. Hu, M. He, Q.S. Chen, R. Liu, Linear stability of thermocapillary liquid layers of a shear-thinning fluid, Phys. Fluids 29 (7) (2017) 073101.

[16] I.A. Frigaard, S.D. Howison, I.J. Sobey, On the stability of Poiseuille flow of a Bingham fluid, J. Fluid Mech. 263 (1994) 133.

[17] E. Ghorbel, A viscoplastic constitutive model for polymeric materials, Int. J. Plasticity 24 (11) (2008) 2032–2058.

[18] N.J. Balmforth, I.A. Frigaard, G. Ovarlez, Yielding to stress: recent developments in viscoplastic fluid mechanics, Annu. Rev. Fluid Mech. 46 (2014) 121–146.

[19] N.J. Balmforth, A.S. Burbidge, R.V. Craster, J. Salzig, A. Shen, Visco-plastic models of isothermal lava domes, J. Fluid Mech. 403 (2000) 37–65.

[20] R. Byron-Bird, G.C. Dai, B.J. Yarusso, The rheology and flow of viscoplastic materials, Rev. Chem. Eng. 1 (1) (1983) 1–70.

[21] R.R. Huilgol, N. Phan-Thien, Fluid Mechanics of Viscoplasticity, Springer, Berlin-Heidelberg, 2015.

[22] C. Nouar, I.A. Frigaard, Nonlinear stability of Poiseuille flow of a Bingham fluid: theoretical results and comparison with phenomenological criteria, J. Non-Newton. Fluid Mech. 100 (1) (2001) 127–149.

[23] I. Frigaard, C. Nouar, On three-dimensional linear stability of Poiseuille flow of Bingham fluids, Phys. Fluids 15 (10) (2003) 2843–2851.

[24] C. Nouar, N. Kabouya, J. Dusek, M. Mamou, Modal and non-modal linear stability of the plane Bingham-Poiseuille flow, J. Fluid Mech. 577 (2007) 211–239.

[25] C. Nouar, A. Bottaro, Stability of the flow of a Bingham fluid in a channel: eigenvalue sensitivity, minimal defects and scaling laws of transition, J. Fluid Mech. 642 (2010) 349–372.

[26] J. Peng, K.Q. Zhu, Linear stability of Bingham fluids in spiral Couette flow, J. Fluid Mech. 512 (2004) 21–45.

[27] M.P. Landry, I.A. Frigaard, D.M. Martinez, Stability and instability of Taylor-Couette flows of a Bingham fluid, J. Fluid Mech. 560 (2006) 321–353.

[28] M.K. Smith, S.H. Davis, Instabilities of dynamic thermocapillary liquid layers. Part 1. Convective instabilities, J. Fluid Mech. 132 (1983) 119–144.

[29] R.J. Riley, G.P. Neitzel, Instability of thermocapillary–buoyancy convection in shallow layers. Part 1. Characterization of steady and oscillatory instabilities, J. Fluid Mech. 359 (1998) 143–164.

[30] Y.R. Li, N. Imaishi, T. Azami, T. Hibiya, Three-dimensional oscillatory flow in a thin annular pool of silicon melt, J. Cryst. Growth 260 (2004) 28–42.

[31] A.K. Babel, B. Cao, G.A. Campbell, On the application of a viscoplastic elastic model to uniaxial elongational flow, J. Plast. Film Sheet. 9 (3) (1993) 224–245.

[32] G.T. Dee, B.B. Sauer, The surface tension of polymer liquids, Adv. Phys. 47 (2) (1998) 161–205.

[33] C.L. Chan, C.F. Chen, Effect of gravity on the stability of thermocapillary convection in a horizontal fluid layer, J. Fluid Mech. 647 (2010) 91–103.

[34] P.J. Schmid, D.S. Henningson, Stability and Transition in Shear Flows, Springer, 2001.